

# The impact of climate change on the wave climate in the Gulf of St. Lawrence

Lei Wang, Will Perrie\*, Zhenxia Long, Maryna Blokhina, Guosheng Zhang, Bash Toulany, Minghong Zhang

Fisheries and Oceans Canada, Bedford Institute of Oceanography, Dartmouth, NS, Canada

## ARTICLE INFO

### Keywords:

Waves  
Climate change  
Storms  
Sea ice  
Extreme value analysis  
Gulf of St. Lawrence

## ABSTRACT

The purpose of this study is to investigate possible local changes in the wave climate for the coastal waters off eastern Canada, particularly in the Gulf of St. Lawrence (GSL) related to changes in marine winds, storm and the sea ice climate, due to climate change. These analyses are based on application of a dynamical downscaling approach whereby a regional climate model is driven by climate change estimates from the Canadian Global Climate Model (CGCM3) to provide relatively high resolution winds to drive a wave model. The CGCM3 simulation follows the A1B climate change scenario of the Special Report on Emission Scenarios from the Fourth Assessment Report (AR4) of the Intergovernmental Panel on Climate Change (IPCC AR4, 2007). The analyses of the wave climate are based on simulations of the waves from a third-generation wave model, WAVEWATCHIII™, and the downscaled winds obtained from the Canadian Regional (atmospheric) Climate Model (CRCM). We show that the significant wave heights in the Gulf of St. Lawrence (hereafter GSL) and neighboring coastal waters will slightly increase in the winter and decrease in the summer, in response to changes in storms and sea ice in the future climate (2040–2069) compared to the present wave climate, represented as 1970–1999. This time period is denoted as the “historical” wave climate in this study. In summer, the changes in significant wave heights ( $H_s$ ) are associated with estimated decreases in the frequency of the occurrence of the cyclones. Projected changes in return values for summer extremes in the wave climate are consistent with the associated changes in the maximum  $H_s$  values. In winter, the projected increases in return values are mostly concentrated in the St. Lawrence Estuary, the northern and southwestern GSL, consistent with changes in the maximum waves in these regions. An important factor related to change in the winter wave climate is change in the sea ice.

## 1. Introduction

Waves are generated by wind, very often in association with storms; if sea ice is present, it will tend to dampen the waves. The GSL (Gulf of St. Lawrence) is a semi-enclosed sea, adjoining the East Coast region of Canada. It has special climate characteristics, because it is partially covered by sea ice in winter and it can be affected by strong storms moving from west to east, as well as nor'easters moving along the eastern coast of North America from Cape Hatteras towards Newfoundland and onwards to Europe, and extra-tropical hurricanes, moving from the southwest towards the northeast, along the eastern coast of North America. In the GSL, the waves can impact society by their potential to damage coastal infrastructure, as well as vulnerable near-shore and offshore structures, marine transport, recreational activities and commercial fishing.

The possible impacts of climate change on waves, including effects

on sea ice, wind and storms, have been investigated by several recent studies (Wang and Swail, 2006; Grabemann and Weisse, 2008; Kharif et al., 2008; Wang et al., 2012; Guo et al., 2015; Ruest et al., 2016). Changes in storm activity in the North Atlantic can affect the winds, which are drivers for changes in the climate of the waves (e.g., Wang and Swail, 2006; Wolf and Woolf, 2006; Guo et al., 2015). Sea ice influences the wave climate mainly through dissipation of the wave energy as waves propagate into the ice, and by directly modifying the open water fetch distance for wind-wave generation and development (Tolman, 2003; Thomson et al., 2016; Shen et al., 2018). Global warming is expected to result in a reduction in sea ice in the GSL, a decrease in extreme winds over large areas of the North Atlantic and a poleward shift in storm tracks in the mid-latitude North Atlantic region, as suggested by climate model simulations (Knippertz et al., 2000; Fischer-Bruns et al., 2005; Yin, 2005; Bengtsson et al., 2006; Lorenz and DeWeaver, 2007; McInnes et al., 2011; Guo et al., 2015; Long et al.,

\* Corresponding author.

E-mail address: [perriew@dfo-mpo.gc.ca](mailto:perriew@dfo-mpo.gc.ca) (W. Perrie).

<https://doi.org/10.1016/j.ocemod.2018.06.003>

Received 19 May 2017; Received in revised form 15 June 2018; Accepted 26 June 2018

Available online 30 June 2018

1463-5003/ Crown Copyright © 2018 Published by Elsevier Ltd. All rights reserved.

2015; Ruest et al., 2016). However, Gallagher et al. (2016) analysed two future climate scenarios (RCP4.5 and RCP8.5) and found a mixed picture for the seasonal mean 10 m winds for the North Atlantic region, suggesting a *decrease* in future *summer* winds over Eastern Canadian coastal areas, with *negligible* changes in estimates for *future* winter winds in these areas. But there are additional factors like sea ice, and therefore it is important to estimate the possible impacts to the wave climate of climate change and the role of these related factors.

Several studies have investigated the mean and extreme wave climate in the Northwest Atlantic and the GSL (Swail et al., 2006; Ruest et al., 2013; Guo and Sheng, 2015; Ruest et al., 2016). Based on wave simulations, Swail et al. (2006) estimated the annual mean and extremes of significant wave heights ( $H_s$ ) in the GSL for the period 1955–2004. They found that the maximum annual mean wave height, the maximum 99% percentile wave heights and the highest percentage of days (during a year) with  $H_s$  exceeding 3 m occur mostly in deep offshore waters, whereas the  $H_s$  values in near shore areas are relative low. Swail et al. (2006) used the Gumbel extremal distribution to estimate the 100-year return period for wave heights. They showed that the 100-year wave height varies from under 6 m in some coastal regions to over 17 m in the deep offshore waters off Eastern Canada. Guo and Sheng (2015) also estimated the 50-year return period for wave heights using the generalized Pareto distribution (GPD) and demonstrated that the highest values are about 14 m in offshore areas, beyond the continental shelf break, but decrease in the coastal regions of the Grand Banks and Scotian Shelf. Compared to the results of Guo and Sheng (2015), the results for the 50-year return period for  $H_s$  over the southwestern part of the GSL estimated by Ruest et al. (2013) are relative high, possibly because the latter did not consider the winter sea ice in simulating the waves. Sea ice is projected to be notably reduced in the GSL by the end of the 21st century. In response to changes in ice, wave heights are expected to increase in this region in projections of the future climate (Ruest et al., 2016). Thus, the impact of sea ice on the winter wave climate needs to be considered.

These studies focus on the *annual* mean and extreme wave statistics in the GSL. The climate features related to *seasonal* mean and seasonal extreme waves in the GSL and discussion of the possible reasons behind these changes have received less investigation. Although Ruest et al. (2016) investigated the impact of sea ice cover on extreme waves, they focused on a limited region of the northwestern GSL and the St. Lawrence Estuary. The impacts of climate change over other areas of this region including the southern GSL around Prince Edward Island, and the eastern GSL near Newfoundland are still not explored. In this study, we investigate the impacts of future climate change on seasonal mean and seasonal extreme waves in the GSL; winter (January–February–March) and summer (July–August–September) estimates are projected separately. We also present a discussion of possible factors that may lead to these future climate changes. This study takes account of the impact of winter sea ice. In addition, the POT method is used to estimate the 10-, 50- and 100-year significant wave heights.

The objective of this study is to investigate the impacts of climate change on the significant wave heights, related winds, storm and sea ice properties in the Gulf of St Lawrence and nearby coastal areas of the Northwest North Atlantic. Waves are driven by winds, which are often generated by storms. The impacts of climate change are experienced by storm activity and sea ice in the Western North Atlantic and thus are exhibited in the wave climate. Sections 2 and 3 describe the models, the data and the relevant methods used in this study. Section 4 gives validations of the simulations of the storms and significant wave heights in terms of the reanalysis data. In Section 5, we discuss the impacts of climate change projections on storms, sea ice and the significant wave heights. Analysis of extreme waves is given in Section 6. Discussion and conclusions are given in Section 7.

## 2. Models and data

### 2.1. Atmospheric winds

In this study, we use the Canadian Regional Climate model (CRCM), version 3.7.1 (Tanguay et al., 1990; Caya and Laprise, 1999) for simulations of the winds to drive the wave model. The computational domain covers much of the eastern North American continent and the North Atlantic. CRCM solves the fully elastic nonhydrostatic Euler equations, combining the semi-Lagrangian, semi-implicit mesoscale compressible community (MCC) model dynamical kernel with the atmospheric GCM physics parameterization package from the Canadian Centre for Climate Modelling and Analysis. Thus, CRCM is an important downscaling technique to simulate regional climate for a limited – area regional domain. In the implementation used here, there are  $259 \times 169$  polar stereographic grid points and a relatively fine horizontal resolution of 45 km (at 60°N). Vertically, there are 29 Gal-Chen levels (Gal-Chen and Somerville, 1975) from the ground to 29 km altitude, at the top of the model's implementation. Initial and lateral boundary conditions are taken from outputs of the Coupled Global Climate Model (CGCM3) (T47), which has a horizontal resolution of about  $3.75^\circ$ , so that there are two grid points per truncation wavelength around any great circle. We use a spectral nudging technique in the CRCM to weakly constrain the large-scale fields towards the driving fields from CGCM3 (T47), following Riette and Caya (2002). The time step is 15 min. Details about CRCM are given by Caya and Laprise (1999), Laprise et al. (2003), Caya and Biner (2004), and for application in our model domain, Guo et al. (2015).

In this paper, we simulate a 30-year period from 1970 to 1999 to represent the present climate. This time period can be denoted as the “historical” wave climate. Initial and lateral boundary conditions for CRCM are taken from CGCM3 outputs following the A1B scenario from IPCC (2007). This scenario assumes high economic growth and “middle usage” of the energy sources with  $\text{CO}_2$  levels reaching 720 ppm by 2100 (Nakićenović et al., 2000). We also simulate a 30-year period from 2040 to 2069 to represent the associated future climate change scenario, also driven by CGCM3 outputs for the A1B scenario. The sea ice and surface winds at 10 m reference height are interpolated in space to match the WAVEWATCHIII™ (hereafter, WW3) wave model grid every 6 hours. Thus, we use the winds to drive WW3, leading to estimates of the wave climate for present climate conditions and also for the future climate scenario.

### 2.2. Waves

The wave climate for this study is computed by the WW3 wave model (version 3.14, the version available at the time of the study), which is a third-generation spectral model with the ST3 physics parameterizations, as described by Tolman et al. (2002) and Tolman (2009), and it includes the usual source terms, such as energy input by wind, wave dissipation, non-linear wave–wave interactions, and bottom dissipation parameterizations. ST3 was the most advanced parameterization package that was available at the time when this project was started. Later physics formulations like ST4 or ST6 were not yet available. Moreover, Liu et al. (2017) have recently compared the performance of ST3, ST4 and ST6 and suggest that within the uncertainty in the wind forcing fields, all three formulations perform well in simulations of wave parameters generated by hurricane conditions.

The model domain is the North Atlantic ( $20^\circ\text{N}$ – $65^\circ\text{N}$ ,  $85^\circ\text{W}$ – $10^\circ\text{W}$ ). The wave model grid spacing is  $0.5^\circ \times 0.5^\circ$ , and the spectral domain is divided into 29 frequency and 24 directional bins ( $15^\circ$ ). Discrete frequency bins range from 0.0418 to 0.6028 Hz, using an increment factor of 1.10. This domain is nested to a higher resolution domain focusing on the GSL ( $42^\circ\text{N}$ – $55^\circ\text{N}$ ,  $72^\circ\text{W}$ – $50^\circ\text{W}$ ) with wave model grid spacing  $0.125^\circ \times 0.125^\circ$ . Wave simulations using WW3 are driven by CRCM winds from 27 December to 31 March (winter season) and 27 June to

30 September (summer season) for each year during 1970–1999 and 2040–2069, allowing the first five days as spin-up time for the wave model. Preliminary wave-ice interaction processes were also considered, specifically the ICO source term package. Thus, if the ice concentration is  $C\%$  at any grid point in the marginal ice zone, then in the model simulation, the spectral wave energy  $E$  at this grid point becomes  $(1 - C/100) \times E$ . Default values for  $C$  of 25% and 75% were used to denote ice-free conditions, and conditions where sea ice is treated as land, respectively. The input fields for sea ice were obtained from the ice-ocean simulations using NEMO ocean model, as described by Long et al. (2015). Although preliminary experimental routines for representation of the boundary effects of ice on waves were implemented in WW3, as provided by Tolman (2003), wave scattering due to ice floes was not yet available at the time of this study. Boundary conditions at the outermost boundary for the model system are assumed to behave like a solid wall; nothing comes in and the boundary is like a sponge, absorbing all waves crossing to the outside.

### 2.3. Sea ice

Sea ice is important in the study of wave climate and climate change, because sea ice reduces the surface winds, reducing the momentum exchange between the atmosphere and the ocean. Validation studies for sea ice were done by Long et al. (2015), comparing their model simulations with National Snow and Ice Data Center (NSIDC) data (Peng et al., 2013) and suggesting that the simulated sea ice cover and ice volume in the GSL are in good agreement with the observations. Long et al. (2015) used the CANadian OPA (CANOPA) model as adapted by Brickman and Drozdowski (2012), based on the Océan PARallélisé, version 9 model (OPA 9.0; Madec et al., 1998) and the Louvain-la-Neuve ice model, version 2 (LIM2; Fichefet and Morales Maqueda, 1997; Bouillon et al., 2009). Comparisons of sea ice cover from Long et al. (2015) to NSIDC data are shown in Fig. 1. Their simulated sea ice concentrations show seasonal variations whereby the sea ice forms over the shallow waters among the north and west GSL coasts, with the maximum sea ice concentrations occurring in the St. Lawrence Estuary and along the Saguenay Estuary in January, eventually almost covering the entire GSL. Maximum concentrations are reached in February, and then start to retreat back to the Saguenay Estuary in March (Fig. 1). The simulated ice volume in the GSL increases from about 22 km<sup>3</sup> in January to 60 km<sup>3</sup> in March.

### 2.4. Reanalysis data

For validation of present wave climate conditions, we compared our results with those of the wave hindcast from the IOWAGA Project (Integrated Ocean Waves for Geophysical and other Applications) described by Rasche and Ardhuin (2013) for the Northwest Atlantic, with 10 min spatial resolution. This dataset was constructed using WW3 with ST4 physics parameterizations, which is the state-of-the-art parameterization for generation and dissipation of wind waves (Ardhuin et al., 2010). The dataset includes the period from 1990 to 2012 at the time of this study.

We use 6-hourly mean sea level pressure (MSLP) fields from the European Centre for Medium-Range Weather Forecasts' ERA-Interim Reanalysis dataset (Dee et al., 2011) as input to the methodology to detect and track cyclones (described in Section 3.1). ERA-Interim is one of the latest available global reanalysis datasets, based on a four-dimensional data assimilation system. The data is available at a high spectral resolution (T255) about ~79 km, for the time period from 1979 to the present. Strachan et al. (2013) have demonstrated that the North Atlantic cyclone track density can be reliably extracted from the ERA-Interim data.

## 3. Methods

In this section, we introduce three methods needed for investigation of the wave climate and the possible effects of climate change. These methods are cyclone detection, spatial correlation and extreme value analysis. The importance of these methods is: 1) detection and tracking of the extratropical cyclones, 2) validation of the wave model estimates for wave climate results, and 3) prediction of the extreme wave heights for differing intervals such as 10, 50 and 100 year time periods.

### 3.1. Cyclone detection

Extratropical cyclones are detected and tracked using the University of Melbourne automatic cyclone tracking scheme (Murray and Simmonds, 1991a, 1991b; Simmonds and Murray, 1999). This cyclone tracking scheme is chosen due to its good performance compared to other automated tracking schemes (e.g., Raible et al., 2008; Neu et al., 2013). In this scheme, the quasi-Lagrangian perspective of cyclone behavior was used rather than the Eulerian perspective. The automatic cyclone tracking scheme identifies possible cyclones based on the 6-hourly maps of the MSLP fields, by comparing the Laplacian of the pressure to the values at 20 neighboring grid points. After a possible 'candidate' cyclone is identified, the location of the associated pressure minimum is located by using ellipsoidal minimization techniques. To determine the cyclones that are meteorologically significant, the 'candidate' cyclones are tested using a minimum concavity criterion, which requires that the area-averaged Laplacian exceed 0.5 hPa (°latitude)<sup>-2</sup> for closed depressions, or 1.5 hPa (°latitude)<sup>-2</sup>, for open depressions, over a radius of 2° latitude from the apparent cyclone center.

After a set of snapshots of potential cyclones is created, satisfying the selection conditions described above, an algorithm is used to track the individual cyclones in successive 6-hourly maps. This approach makes an estimate of the new position of the each cyclone, calculates the probability of 'associations' between the actual and predicted cyclone positions and then estimates the most probable combination for each single physical cyclone. Thus, the storm track density is defined as the number of cyclone tracks passing through a given grid cell.

Here, 6-hourly MSLP data from regional downscaled CRCM model outputs are used to represent the present climate, while MSLP data from ERA-Interim reanalysis are used for validation. Since spatial resolution of the input data has a strong influence on the number and characteristics of detected cyclones (Jung et al., 2006), both datasets are interpolated to the same polar stereographic grid before making an analysis of cyclones and their tracks. We focus on cyclones that last at least 4 time steps on the 6-hourly maps (i.e., 24 h). The CRCM model grid introduces geographical limits to our study; thus, cyclones are detected and tracked over the North Atlantic (20°N–72°N, 120°W–0.75°W).

### 3.2. Spatial correlation

We adopt statistical metrics to quantitatively evaluate the spatial correlation of the climate variables estimated by models against the observations. Suppose that  $x$ ,  $y$  are simulated and observed data at  $M$  grid points in space, respectively. The spatial correlation  $C$  between  $x$  and  $y$  is defined as:

$$C = \frac{\frac{1}{M} \sum_{m=1}^M (x_m - \bar{x})(y_m - \bar{y})}{std_x std_y} \quad (1)$$

where  $\bar{x}$  and  $\bar{y}$  are the mean of  $x$  and  $y$  over the  $M$  grid points and  $std$  is the spatial standard deviation. The spatial standard deviation of  $x$  is defined as

$$std_x = \sqrt{\frac{1}{M} \sum_{m=1}^M (x_m - \bar{x})^2} \quad (2)$$

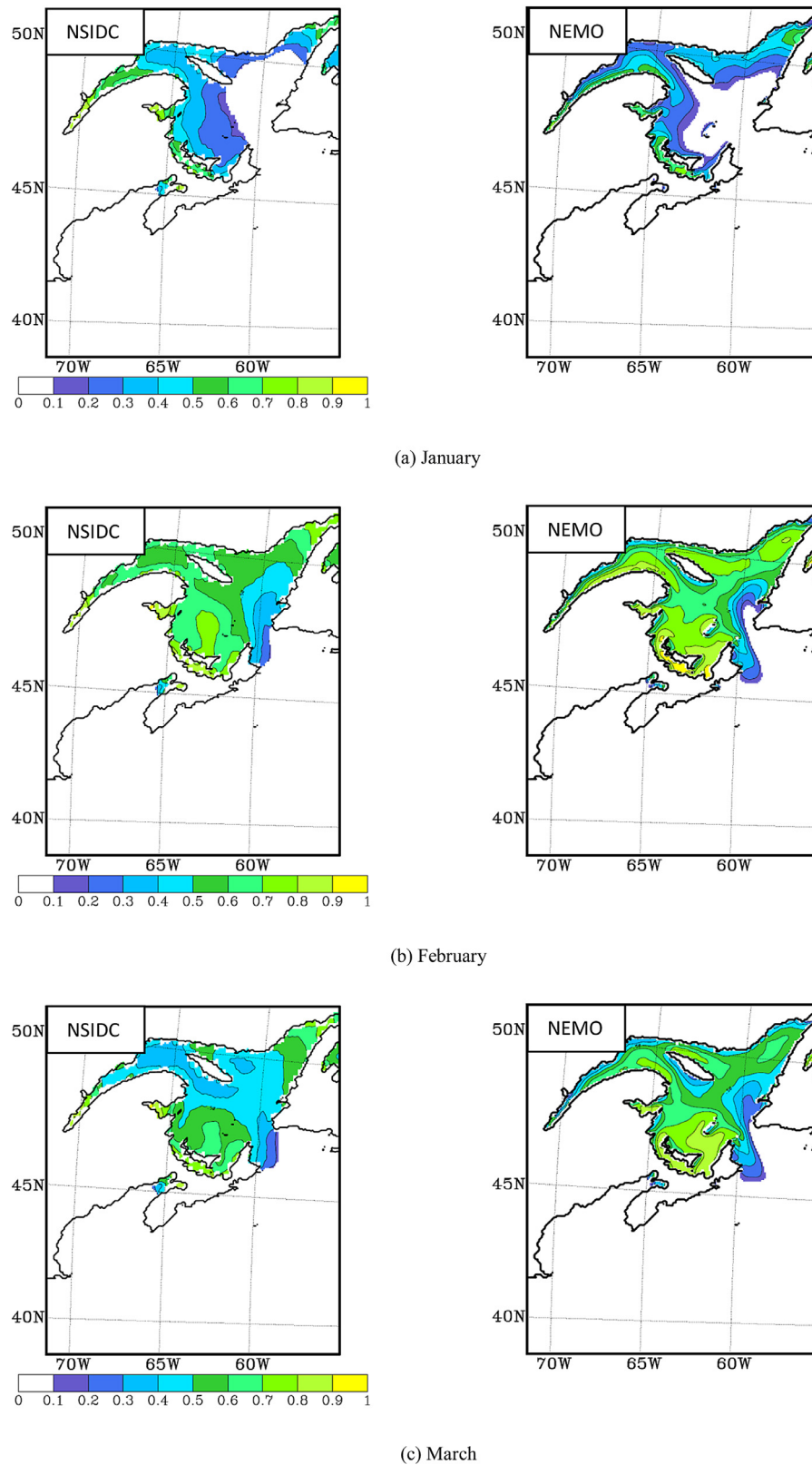


**Fig. 1.** Monthly ice concentration (fraction) from the NEMO model simulation (right), and from NSIDC data (left), averaged for the period 1970–1999: (a) January, (b) February, and (c) March. Color bar indicates concentration as a fraction of unity. From Long et al. (2015). (For interpretation of the references to color in this figure legend, the reader is referred to the web version of this article.)



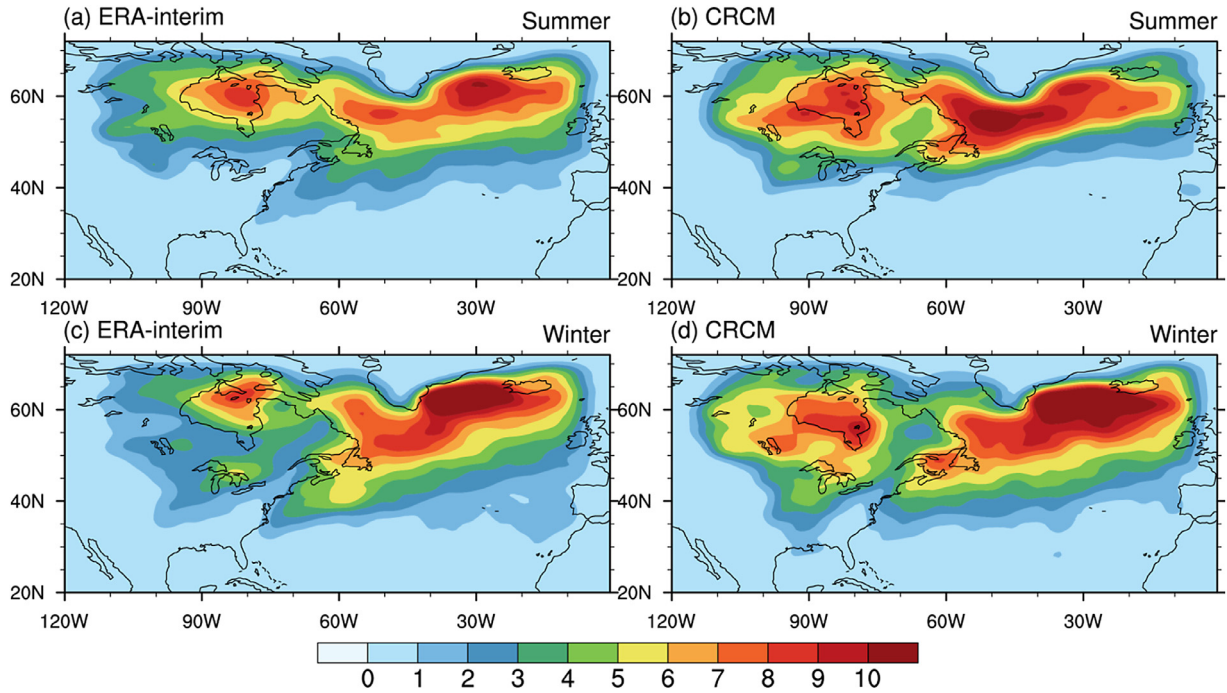


Fig. 2. Summer (July–September, JAS) and winter (January–March, JFM) cyclone track densities (the mean number of cyclone track per unit area per month) in the North Atlantic over the 1979–2008 period: ERA-Interim (left column) and simulated by CRCM (right column).

### 3.3. Extreme value analysis

In extreme value analysis, two statistical approaches are commonly used to obtain the  $R$ -year return period significant wave height (Menéndez et al., 2009; Teena et al., 2012; Ruest et al., al., 2013). These are the annual maxima (AM) method and the peaks-over-threshold (POT) method.

#### 3.3.1. AM method

In the AM method, the maximum values in each year are extracted to construct the dataset that is used for the extreme value analysis. The distribution of the maximum values can be represented approximately by a generalized extreme value distribution (GEV) (Coles, 2001), whose cumulative distribution function is

$$G(z) = \begin{cases} \exp\left\{-\left[1 + \varepsilon\left(\frac{z - \mu}{\sigma}\right)\right]^{-1/\varepsilon}\right\} & \text{for } \varepsilon \neq 0 \\ \exp\left\{-\exp\left[-\left(\frac{z - \mu}{\sigma}\right)\right]\right\} & \text{for } \varepsilon = 0 \end{cases} \quad (3)$$

where  $\mu, \sigma, \varepsilon$  are the location, scale and shape parameters, respectively. The shape parameter can determine the type of distribution. Depending on the value of the shape parameter  $\varepsilon$ , the GEV distribution has three possible distribution families: (1) Gumbel distribution, with  $\varepsilon = 0$ ; (2) Fréchet distribution, with  $\varepsilon > 0$ ; and (3) Weibull distribution, with  $\varepsilon < 0$ . In this paper, the parameters are estimated by the maximum likelihood (ML) method and comparisons are made with the probability weighted moments (PWM) method in order to fit a candidate distribution function to a given sample. The coefficient of determination ( $r^2$ ) and root mean square error (RMSE) are used to identify the best-fit distribution.

In this approach, the return value  $Z_R$  for the  $R$ -year significant wave height is the value exceeded once every  $R$  years on the average. This is obtained by finding the inverse of the function of the cumulative distribution, following Goda (2010):

$$Z_R = G^{-1}\left(1 - \frac{1}{R}\right) \quad (4)$$

where  $R$  is the return period associated with the return value. Here  $R$  is defined as:

$$R = \frac{1}{1 - G(Z)} \quad (5)$$

and therefore, the return value obtained by Eqs. (1) and (2) is expressed as follows:

$$Z_R = \begin{cases} \mu - \frac{\sigma}{\varepsilon} \left\{1 - \left[-\log\left(1 - \frac{1}{R}\right)\right]^{-\varepsilon}\right\} & \text{for } \varepsilon \neq 0 \\ \mu - \sigma \log\left[-\log\left(1 - \frac{1}{R}\right)\right] & \text{for } \varepsilon = 0. \end{cases} \quad (6)$$

#### 3.3.2. POT method

Alternately, another method that can also be used for extreme wave analysis is the POT method, which considers the peaks exceeding a pre-set threshold. In the POT method, the distribution of the threshold excesses is assumed to follow a generalized Pareto distribution (GPD), following Coles (2001). In this approach,  $Z$  is the cluster maxima of the significant wave heights. Given a threshold  $u$ , the cumulative distribution function of GPD can be expressed as:

$$G(z) = \begin{cases} 1 - \left[1 + \frac{\varepsilon(Z - u)}{\sigma}\right]^{-1/\varepsilon} & \text{for } \varepsilon \neq 0 \\ 1 - \exp\left(-\frac{Z - u}{\sigma}\right) & \text{for } \varepsilon = 0 \end{cases} \quad (7)$$

where  $\sigma$  represents the scale parameter and  $\varepsilon$  is the shape parameter. Like the GEV method, the shape parameter determines the type of the distribution. When  $\varepsilon = 0$ , the GPD reduces to an exponential distribution. When  $\varepsilon < 0$ , the GPD distribution becomes the Pareto distribution. Finally, when  $\varepsilon > 0$ , the GPD distribution becomes the beta distribution. The threshold selection methodology is necessary in the GPD method, because the high threshold value reduces the bias but increases

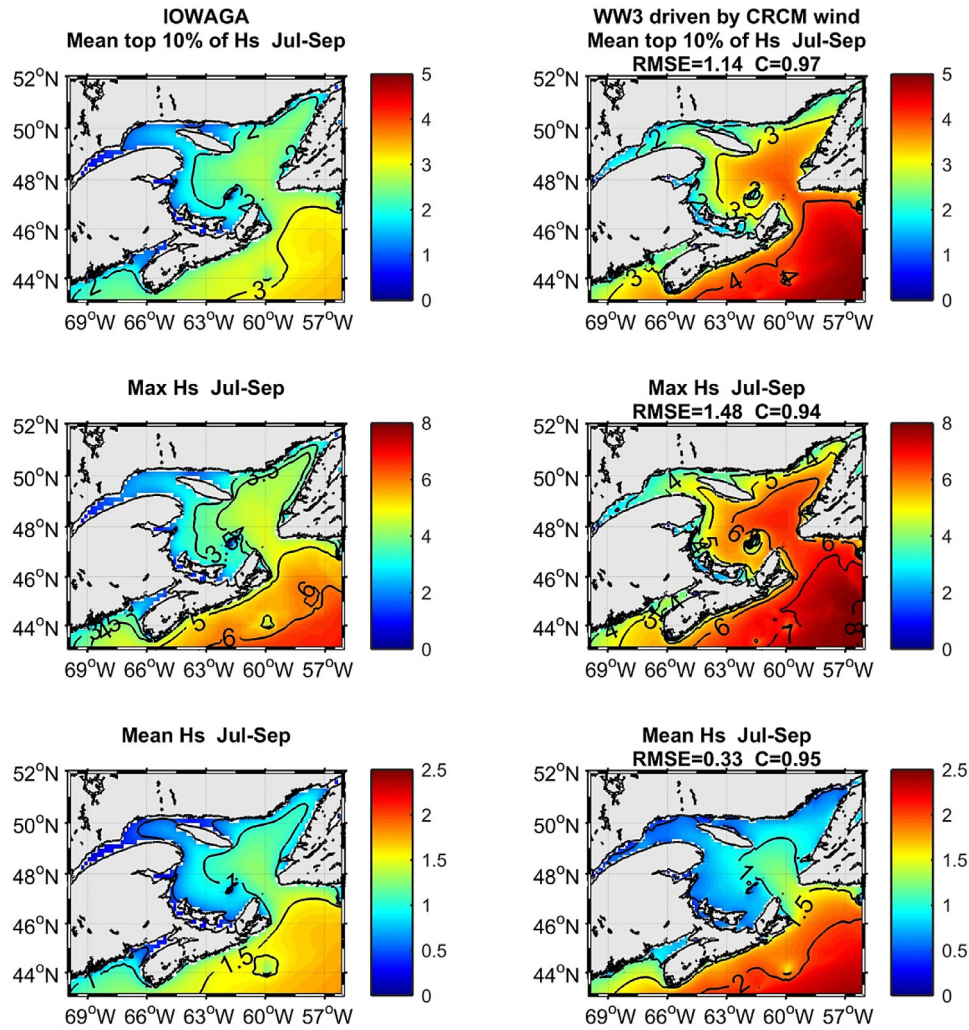


**Fig. 3.** Summer mean of the mean 10% highest (top), maximum (middle), and mean (bottom) significant wave height (m) in the GSL over the 1990–2012 period: IOWAGA (left column) and simulated by WW3 driven by CRCM winds (right column). The root mean square error (RMSE) and the spatial correlation (C) between the IOWAGA simulations and WW3 simulations driven by CRCM winds are shown at the top of each panel (right column).

the uncertainties of the parameter estimation, *whereas* the low threshold gives the opposite result. A sensitivity analysis on threshold selection was performed by Ruest et al. (2013) in application of the POT method in the Gulf of St. Lawrence (GSL). Their results show that estimates of the return values are not sensitive to the choice of the threshold from 90% to 99% percentile. Therefore, we choose 95% and 97% percentile for significant wave heights as the two threshold values. After the threshold has been fixed, the time length between consecutive exceedances of the threshold is set, in order to get independent extreme events. Here, we select a minimum of 48 h as the separation time, following Caries and Sterl (2005) and Teena et al. (2012). Besides the ML and PWM method, the maximum product of spacings (MPS) method is also used for parameter estimation when fitting the GPD.

Therefore, the return value  $Z_R$  of the  $R$ -year significant wave height, corresponding to the POT method is:

$$Z_R = \begin{cases} u + \frac{\sigma [(Rn\xi_u)^\varepsilon - 1]}{\varepsilon} & \text{for } \varepsilon \neq 0 \\ u + \sigma \log(Rn\xi_u) & \text{for } \varepsilon = 0 \end{cases} \quad (8)$$

An estimation of the return value  $Z_R$  is obtained by solving  $\xi_u \left[ 1 + \varepsilon \frac{(Z_R - u)}{\sigma} \right]^{-1/\varepsilon} = \frac{1}{Rn}$  for  $\varepsilon \neq 0$  and  $\xi_u \exp\left(-\frac{Z_R - u}{\sigma}\right) = \frac{1}{Rn}$  for  $\varepsilon = 0$ , where  $n$  is the number of observations per year and  $\xi_u$  is the probability that an individual observation exceeds the threshold, which can be

estimated as

$$\xi_u = \frac{\lambda}{n}. \quad (9)$$

Here, it is assumed that the number of exceedances is approximately Poisson-distributed with respect to the parameter  $\lambda$ .

#### 4. Model validation

As noted in Section 2.1, to represent the present climate, we simulate a 30-year period from 1970 to 1999, which can also be denoted as the “historical” wave climate, in this paper. However, in this section, the simulation is extended to a 43-year period from 1970 to 2012 in order to allow validation with IOWAGA reanalysis wave climate data which is only available from 1990. Validation is carried out with respect to storms and significant wave heights, to evaluate the performance of CRCM, and WW3, driven by CRCM winds.

##### 4.1. Storms

In summer, the cyclone track density derived from ERA-Interim data suggests that the high frequency region for cyclone development appears over the middle and high latitudes (north to 45°N), with a maximum density over the open water area directly southeast of Greenland

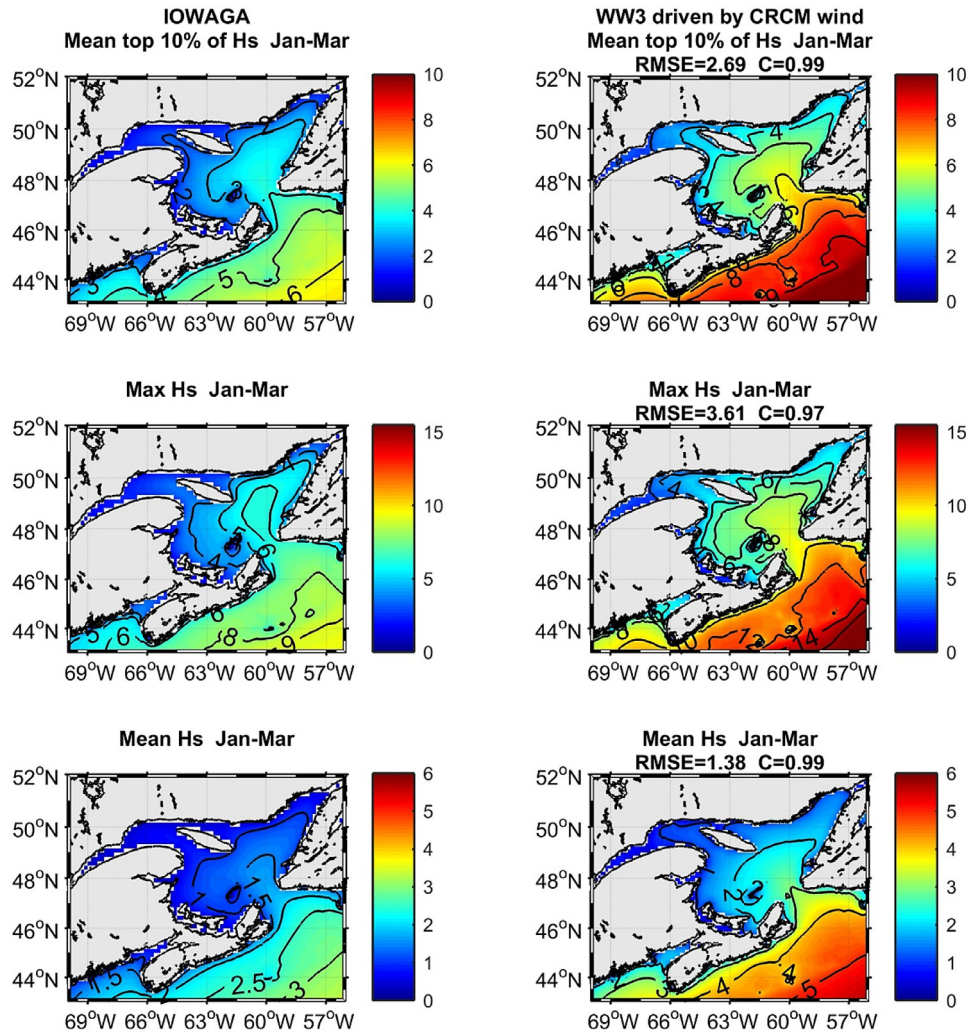


Fig. 4. As in Fig. 3 for the winter season.

(Fig. 2a). By comparison, the CRCM model can capture the overall spatial pattern of track density shown in the ERA-Interim reanalysis data, although the former overestimates the cyclone frequencies south of the tip jet of Greenland (Fig. 2b). The locations of maximum cyclone density are simulated well in the CRCM simulations. However, CRCM overestimates the cyclone activity in the GSL, compared to the estimates from ERA-Interim data.

A similar comparison for the winter season is shown in Fig. 2c and d. For the ERA-Interim data, there are slightly more cyclones over the northeastern North Atlantic and in the GSL than the results in summer (Fig. 2a and c). The maximum cyclone frequencies are mainly located in the open water areas on the east side of Greenland. Overall, the estimated cyclone track density for winter seasonal mean CRCM simulations (Fig. 2d) are in agreement with ERA-Interim results in locations of maximums, magnitudes and spatial patterns of track density. For the GSL, the overestimates from CRCM simulations are found in winter. Similar results are found by the methodology of Guo et al. (2015), which is based on minimum MSLP rather than MSLP gradients used here.

#### 4.2. Waves

The simulated *summer* means for the mean 10% highest, maximum, and mean significant wave heights for the 1990–2012 period from WW3 driven by CRCM winds are compared with the IOWAGA wave

hindcast data in Fig. 3. In general, results from WW3, as driven by CRCM winds and wave data from the IOWAGA simulations show similar spatial patterns; values for mean 10% highest, maximum and mean wave heights are generally *decreasing*, with a gradient from the deep water areas to the shallow water areas. In the summer, the simulated mean significant wave heights (WW3 driven by CRCM winds) are around 0.5–1.3 m in the GSL, while the simulated mean of 10% highest and maximum wave heights are around 2–3.6 m and 3–6.6 m, respectively. Compared to IOWAGA, WW3 (driven by CRCM winds) produces higher values for the mean 10% highest waves as well as the maximum wave heights and reasonable comparisons for mean values. Based on the pattern correlation coefficient (C) and root mean square error (RMSE) shown in each panel, WW3 (driven by CRCM winds) is able to capture the magnitude of the wave heights well, especially the mean values, as well as the spatial patterns; correlation coefficients are in excess of 0.9.

In *winter*, our simulated WW3 results for mean 10% highest, maximum, and significant wave climate exhibit similar spatial patterns as those found in summer, although the values are relatively higher as presented in Fig. 4. The simulated mean significant wave heights are around 1–3.5 m in the GSL, and the wave heights for winter mean of the mean 10% highest and maximum, are around 2–7 m and 3–10 m, respectively. WW3 driven by CRCM winds overestimates the mean 10% highest, the maximum and mean wave heights, compared to the IOWAGA simulations, but consistently captures the spatial patterns well,



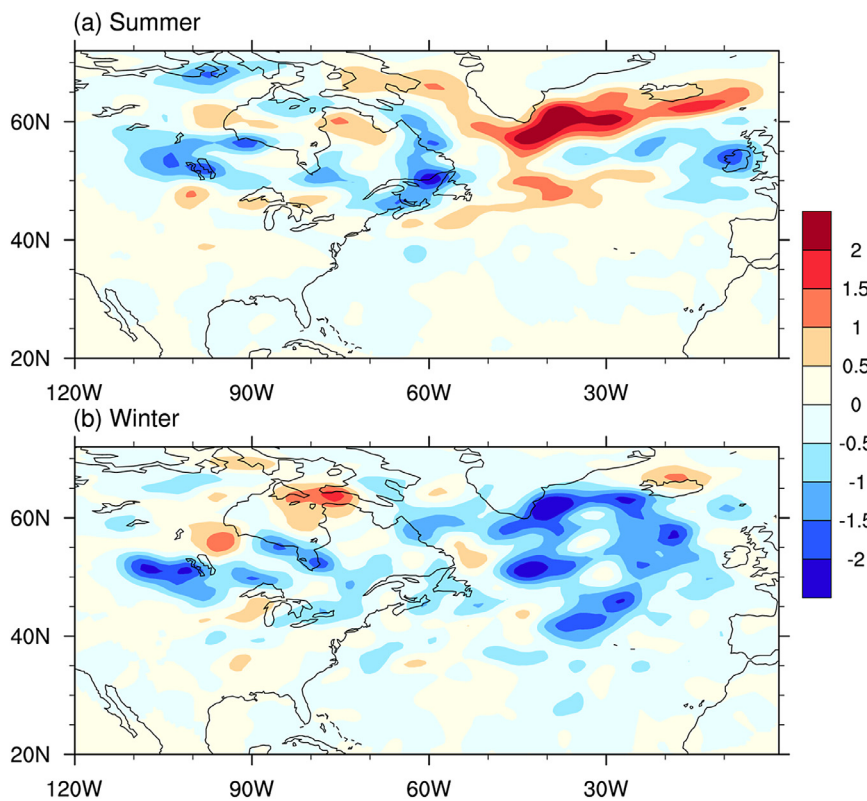


**Fig. 5.** Changes in the summer (top) and winter (bottom) cyclone track density (the mean number of cyclone tracks per unit area per month) in the North Atlantic from the CRCM model simulation for the SRES A1B scenario for the period 2040–2069 relative to the historical simulation for the present climate represented as 1970–1999.

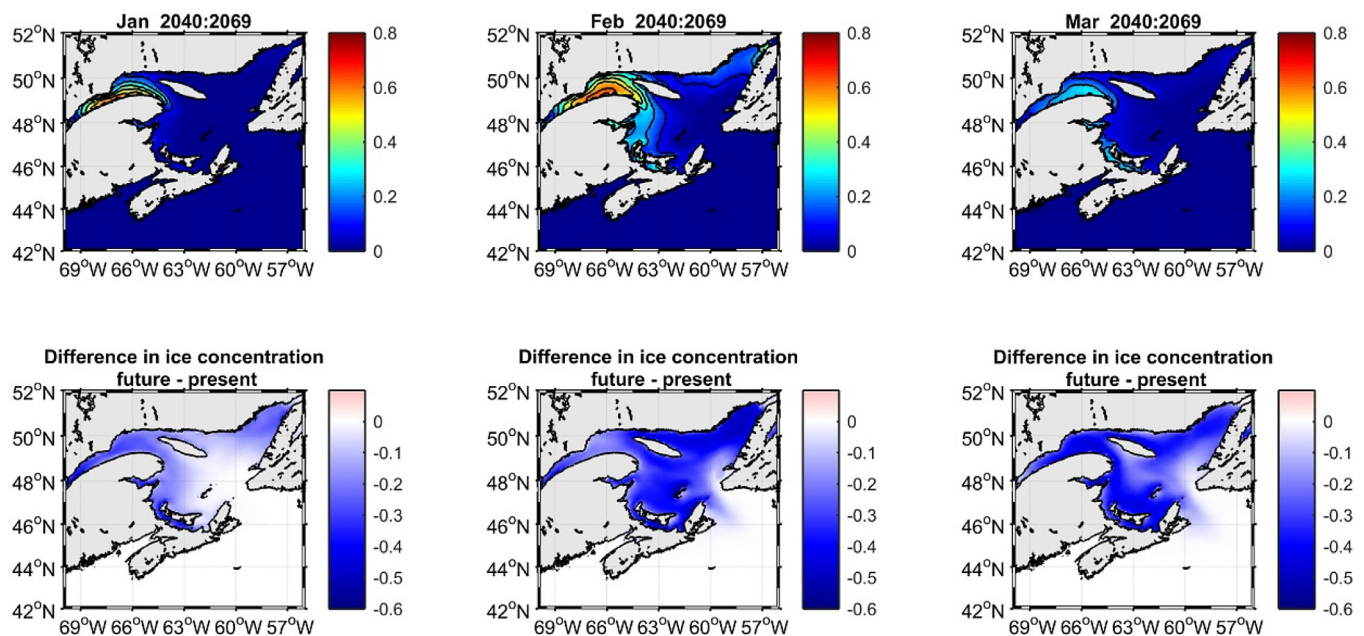


**Fig. 6.** The sea ice concentration for each month of the winter season (Jan., Feb., Mar.) for the estimated future climate period 2040–2069 (upper panels) and future changes in sea ice concentration compared to corresponding conditions for the present climate period 1970–1999 (lower panels).

with spatial correlations higher than 0.96. As illustrated from the RMSE values in each panel, the values of mean 10% highest and maximum wave heights estimated by WW3 have larger differences than those of mean wave heights, when compared with results from IOWAGA simulations.

## 5. Climate change impacts

### 5.1. Storms

In this section, we focus on summer and winter seasons. The differences in cyclone track density between the future climate scenario



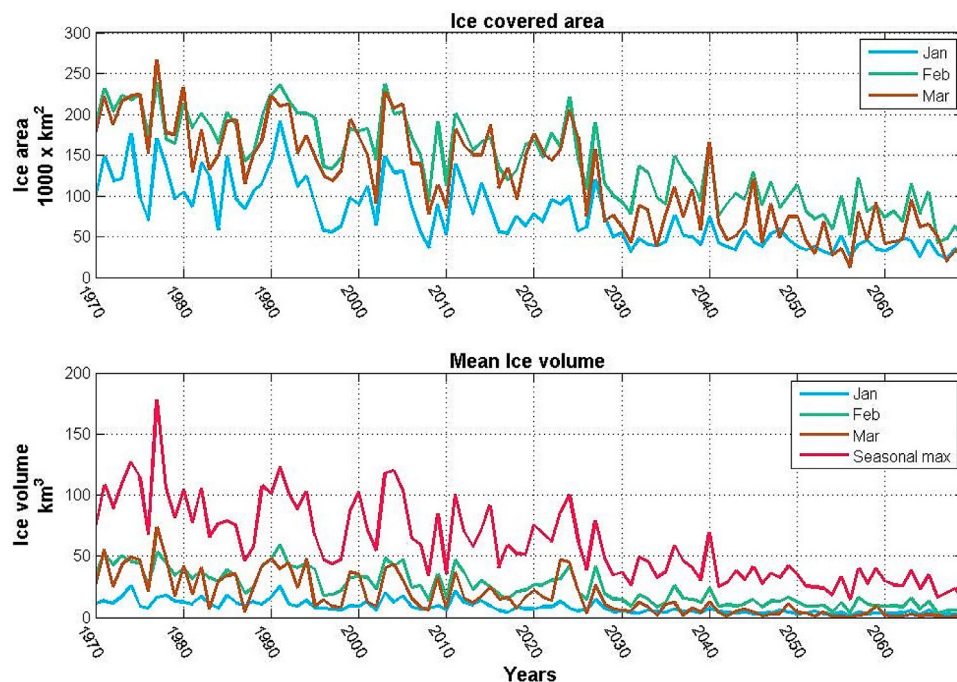


Fig. 7. Estimated sea ice cover (top) and mean ice volume (bottom) in the Gulf of St. Lawrence for each month of the winter season over time, from the present to the estimated future climate (1970–2069). The seasonal maximum ice volume is added in the bottom panel, denoted by the pink line. (For interpretation of the references to color in this figure legend, the reader is referred to the web version of this article.)

considered in this study and the historical simulations for these two seasons, are shown in Fig. 5. In summer, for the future climate change scenario, a significant increase in cyclone track density is projected to occur off the coasts of Greenland and Iceland with an apparent decrease in the Labrador Sea, in the GSL and over the Northeast Atlantic and extending to Western Europe (Fig. 5a). The projected poleward shift in the summer cyclone track density and the estimated decrease in cyclones in the GSL are in agreement with the estimates based on the ECHAM5 coupled climate model by Bengtsson et al. (2006). In winter, the CRCM simulations suggest that the cyclone track density decreases in the areas off Greenland and Iceland, as well as in the GSL region, with slight increases in track density off the coast of Newfoundland (Fig. 5b).

## 5.2. Sea ice

Ruest et al. (2016) study the influence of sea ice on significant wave heights. Their results show that extreme values for  $H_s$  in the GSL during 1981–2010 are reduced by about 12% through the effects of sea ice. Therefore, extreme values for  $H_s$  are expected to increase in the late 21st century due to the reduction in sea ice. However the area of their interest was limited to the northwestern part of the GSL only. Considering the sea ice formation and melt processes during the winter shown in Fig. 1, we investigate possible future changes in sea ice concentration over the GSL for each month of the winter season for the A1B climate scenario during 2040–2069, relative to the present climate period 1970–1999 (Fig. 6). In the A1B climate scenario, the area covered by ice becomes smaller in each winter month, compared to the present climate. March is notable because the GSL is estimated to be virtually ice free in the future climate scenario. A prominent feature in ice changes is that there is a slight decrease in ice over the shallow waters adjoining the coast in January and a significant decrease over nearly the entire GSL in both February and March.

The reduction in GSL sea ice is also suggested by the time series in Fig. 7 showing the changes in sea ice cover and ice volume from the present to the future climate scenario. Declining trends for sea ice cover area are apparent, particularly after the late 2020s in each month. The decrease in sea ice cover area is approximately 80% in the 2060s compared to the 1970s, for each month. The area covered with ice in

January is smaller than the areas estimated for February and March for the entire time period. The estimated mean ice volume shows similar steady decreases, as with reductions in ice cover in the GSL. The most remarkable decreases are estimated to occur after the late 2020s, in all three months. The seasonal maximum ice volume changes from around 100 km<sup>3</sup> during the 1970s to about 25 km<sup>3</sup> during the 2060s.

## 5.3. Waves

For summer conditions, the projected changes in mean  $H_s$ , maximum and mean of top 10%  $H_s$  for 2040–2069 relative to the present climate (1970–1999) are shown in Fig. 8. Overall, the decrease of mean, maximum and mean top 10% wave heights over areas of the GSL, follow the projected poleward shift of the summer cyclone track density mentioned in the previous section. Therefore, a decrease in cyclone activity in the GSL should be expected to contribute to decreases in the estimated mean  $H_s$ , maximum and mean top 10%  $H_s$  in the summer seasons of the future climate scenario. However, there are a few small areas where waves are estimated to increase in the future climate. Relatively weak increases in maximum  $H_s$  are estimated to occur for small areas of Jacques Cartier Strait, the St. Lawrence Estuary and the southern GSL reflecting the related changes in the winds and cyclone tracks.

For winter conditions, the changes in mean  $H_s$  for each winter month are different. We show the changes in mean  $H_s$  for each month for the period 2040–2069 minus present climate conditions (1970–1999) in Fig. 9. This figure also shows the projected changes in maximum and mean of 10% highest  $H_s$ . It can be seen that in each month the changes in mean  $H_s$  share similar spatial patterns as those of the mean of 10% highest  $H_s$  and maximum  $H_s$  in the GSL. The projected changes in January are different from those of February and March. In January, there are slight increases in mean  $H_s$ , maximum and mean of top 10%  $H_s$  over the St. Lawrence Estuary, the northeast GSL and waters leading to the Belle Isle Strait and to a lesser extent, the western GSL. By comparison, in February and March, the significant increases in these variables are suggested to occur over the entire GSL.

For the wave climate in winter, the two dominating factors are the impacts of climate change on cyclones and their tracks, and on sea ice. In winter, the cyclone track density is projected to decrease in the GSL.

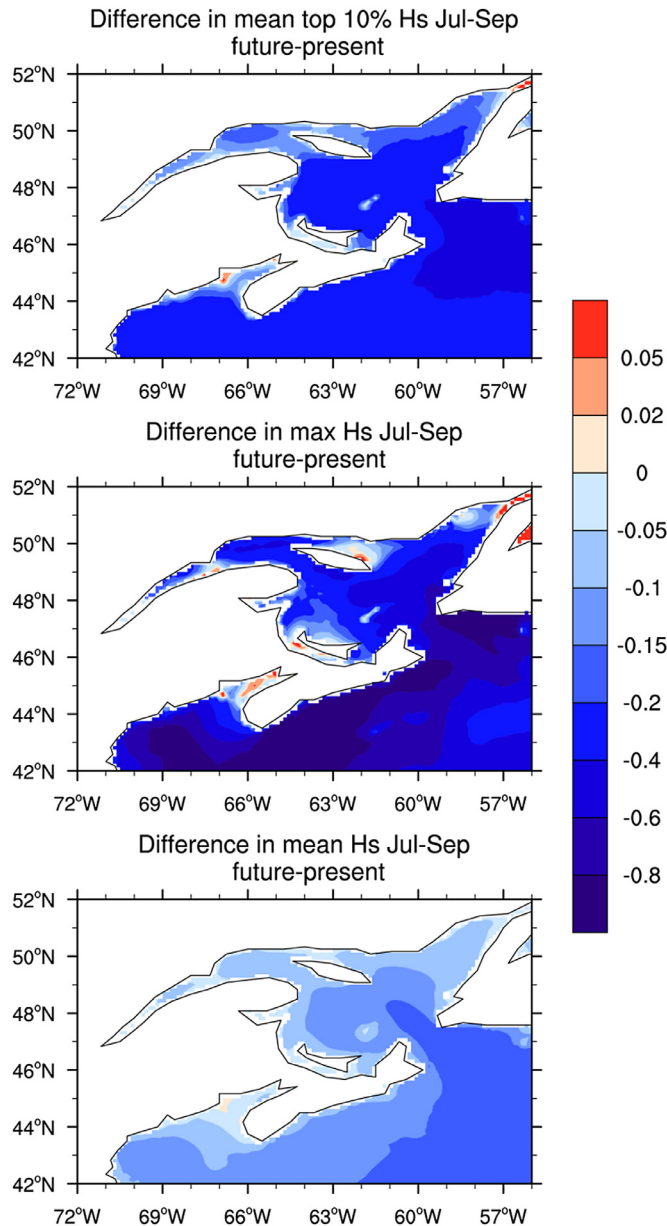


**Fig. 8.** Changes in the mean top 10% of highest waves, maximum  $H_s$  and mean  $H_s$  (m) in the Gulf of St. Lawrence, in summer, for A1B climate change scenario for the period 2040–2069, relative to present climate represented as 1970–1999.

Generally, less cyclone activity implies decreased estimates for  $H_s$  in the climate change scenario. However, this seems not to be the dominant process in our study. On the contrary, Fig. 1 suggests that the sea ice experiences changes in the formation and melt processes from January to March, relative to the present climate. These changes are progressive and significantly affect the associated wave climate, at each phase of the seasonal cycle, because wave-ice interactions affect the attenuation of the wave climate (Section 2.2), and the spatial distribution of sea ice concentration in the GSL is different in each month. Moreover, in the climate change scenario, changes in sea ice are also different, month by month (Fig. 6).

To address the role that sea ice plays in wave climate in winter, we have presented the changes in the wave climate month by month. Compositely, the seasonal mean  $H_s$ , of maximum and of mean 10% highest  $H_s$ , are projected to increase in the GSL. Therefore, the influence of climate change on the cyclones and thus on the winter wave

climate is mitigated by changes in sea ice. Here, we consider the influence of ice on the GSL wave climate by comparing the change patterns for waves and sea ice. Comparing Figs. 6 and 9, it is apparently that the changes in mean  $H_s$ , mean 10% highest and maximum  $H_s$  are consistent with changes in sea ice for each winter month, in the GSL. Therefore, reductions in sea ice are a determining factor that results in increased waves in the future climate scenario, as shown in mean, maximum and mean top 10% waves estimates in the GSL.

## 6. Extreme wave analysis

In performing an extreme value analysis, variations in the steps used in the methodology can lead to differing results. Considerations include: the choice of the extreme value distributions (GEV family or GPD family), the threshold selection for GPD (95% or 97% quantile) and the choice of methods to estimate the parameter to fit a candidate distribution (MPS, ML or PWM). In this study, we considered several combinations mentioned above and we adopted the  $r^2$  (coefficient of determination) and root mean square error (RMSE) to estimate differing distributions with respect to the model data (see Table 1):  $r^2$  is a measure of how well a given distribution can fit the data. The values of  $r^2$  range from 0 to 1, where higher values indicate better fits. In contrast, RMSE is used to measure the differences between values estimated by the differing distributions and the values of the original data. Lower values of RMSE indicate better fits to the data. We note that estimates of the return value have been shown to not be sensitive to the choice of the threshold, from 90% to 99% percentile, by Ruest et al. (2013).

There can be large differences between statistical results obtained by using the GEV model or the GPD model in the GSL in summer, as illustrated in Table 1. The values of  $r^2$  resulting from GPD are all larger than 0.9, whereas  $r^2$  resulting from GEV are lower than 0.9. Similar results are obtained for RMSE values. Lower RMSE values are obtained using GPD and higher values are estimated from GEV. These results indicate that the GPD distribution fits the summer GSL data better than the GEV distribution. In the GPD results, the 95% percentile for  $H_s$  is shown (Table 1) as a suitable threshold value for extreme wave analysis with a better performance for the fitted GPD, compared to the GPD results with 97% percentile threshold. Therefore, a GPD approach is applied to determine the 95% percentile as the threshold; we choose the ML method to estimate the GPD parameters. This methodology is treated as the best-fit distribution to estimate the R-year return period significant wave heights. As shown by the results for summer, the GEV model is not the best candidate for fitting the distribution for the winter extreme  $H_s$  when compared to the GPD model, because the  $r^2$  values resulting from GEV are relatively low and the RMSE values are relatively high. Comparing the statistical analysis obtained from the two thresholds and three methods to estimate the parameters in GPD, we find that the 95% percentile threshold and the ML method are the best choice for fitting the distribution for the winter extreme  $H_s$ .

The 10-, 50- and 100-year estimates for extreme values for  $H_s$  are calculated by using the GPD model with 95% percentile threshold and the ML method for the 30 year time slice. These estimates are achieved separately for the present climate, represented as 1970–1999 (also denoted as “historical”), and for the future climate scenario, 2040–2069. Fig. 10 displays the summer 10-, 50- and 100-year extreme values for  $H_s$  in the GSL for 1970–1999. In the present climate, the spatial patterns of the 10-, 50- and 100-year extreme values for  $H_s$  are similar to each other. The most severe extreme waves are located off-shore, in open ocean waters and decrease in moving to the coastal areas.

At the center of the GSL, the summer 10-, 50- and 100-year extreme values for  $H_s$  are around 7–9 m, 7–10 m and 7–11 m, respectively. By comparison, in the open ocean, the most severe extreme waves are more than 10 m, 12 m and 13 m, respectively, for each return level. Fig. 10 also shows the difference between the future climate scenario and the present climate. In the future, the patterns of change in 10-, 50-

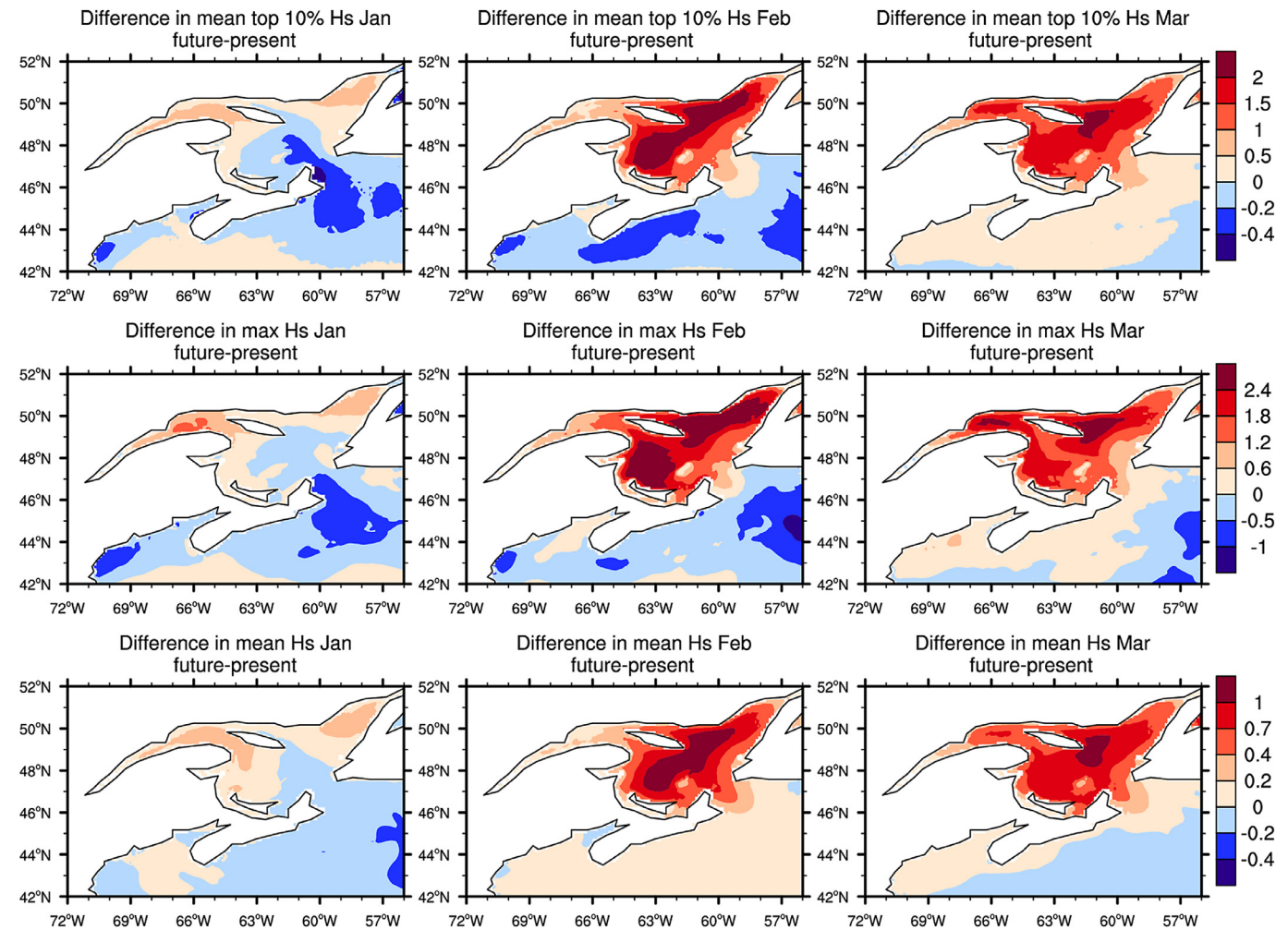


Fig. 9. As in Fig. 8, for January (left), February (middle) and March (right).

**Table 1**  
Statistical analysis of characteristics of the distributions and their fit to the data for summer and winter estimates.

Distribution	Method	$r^2$ summer/winter	RMSE summer/winter
GPD 95%	MPS	0.9429/0.9543	0.2355/0.2639
<b>GPD 95%</b>	<b>ML</b>	<b>0.9581/0.9640</b>	<b>0.2062/0.2380</b>
GPD 95%	PWM	0.9526/0.9592	0.2095/0.2438
GPD 97%	MPS	0.9152/0.9310	0.2953/0.3104
GPD 97%	ML	0.9407/0.9495	0.2543/0.2711
GPD 97%	PWM	0.9283/0.9405	0.2604/0.2838
GEV	ML	0.6920/0.6055	0.7671/0.9018
GEV	PWM	0.6425/0.4974	0.7619/0.8857

and 100-year extreme values for  $H_s$  are similar to each other; however, with slight exceptions, the areas with increased return values of extremes in  $H_s$  are enlarged from corresponding distributions of the 10-year  $H_s$  to 100-year  $H_s$ , such as the St. Lawrence Estuary, Jacques Cartier Strait and the southwestern part of the GSL.

In the regions mentioned above, projected increases in the return values of extremes in  $H_s$  (Fig. 10) are consistent with the areas where there are projected increases in maximum  $H_s$  (Fig. 8), although the former are estimated to cover larger areas than the latter. However, as shown in Fig. 10, other regions are projected to decrease in terms of their return values. The change amplitude of the decreases in extremes increases gradually, in going from the coastal area to the open ocean. The maximum amplitudes of the decreases in  $H_s$  are about 1.5 m, 2 m

and 2 m for the 10-, 50- and 100-year extreme values, respectively.

In winter, the estimated return values of extreme values of  $H_s$  are higher than those in summer, as shown in Fig. 11. The distribution of extreme waves in winter is characterized by the gradient decreases in  $H_s$  from the offshore open ocean waters to the coastal areas. The large values of the 10-, 50- and 100-year extremes in  $H_s$  in the GSL are approximately 11 m, 13 m and 13 m, respectively. The return values over the St. Lawrence Estuary and the southwestern GSL are around 0–5 m and over the northern GSL, 5–7 m. Like the results in summer, the spatial patterns of the corresponding results in winters, for 10-, 50- and 100-year extremes in  $H_s$  for the middle of the 21st century (2040–2069) are similar to each other. However, the projected increases in return values are mostly concentrated over the northern GSL, with maximum amplitudes that are above 1 m for 10-year extremes in  $H_s$  and above 2 m for 50- and 100-year extremes in  $H_s$ . These results are consistent with the areas where increases in maximum  $H_s$  are projected to occur in the future climate scenario. Moreover, decreases in return values are located in the central and rather large portions of the southern GSL, with the maximal amplitudes above 0.5 m for the central GSL for 10-year extremes in  $H_s$  and above 2 m over the GSL west coast area for 50- and 100-year extremes. Note that this is contrary to the projected maximum  $H_s$  values for the same region.

To test the credibility of the return values estimated by GPD, we use the GEV distribution, again fitted by the ML method, to obtain the 10-, 50- and 100-year extreme values in  $H_s$  for both present and future climates (figures not shown). In the present climate, the return values estimated by the GEV distribution have values that are similar to those



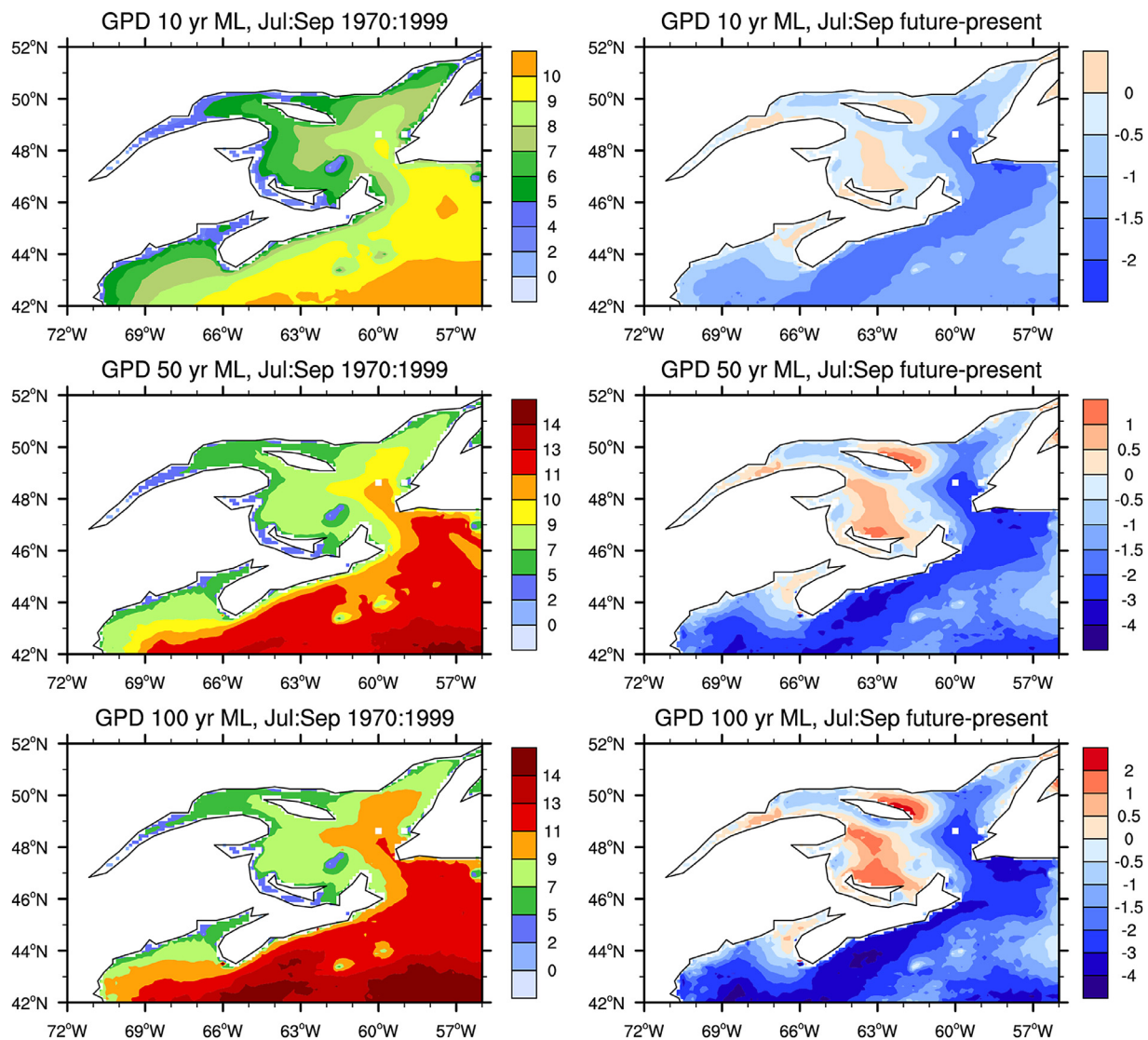


**Fig. 10.** Estimated summer 10-, 50- and 100-year extremes for  $H_s$  (m) computed from 30 year wave simulations (summer: July to September) driven by winds from CRCM: for present climate 1970–1999 (left panels) and the changes in the summer 10-, 50- and 100-year extremes for  $H_s$  (m) for A1B scenario for 2040–2069 minus the present climate (right panels).

obtained with the GPD method, both in spatial patterns and in the amplitudes of the estimates. However, the GEV estimates for  $H_s$  in summer are slightly higher for the 50- and 100-year extremes over the waters approaching Cabot Strait compared to the corresponding estimates from GPD. It is also found that GEV estimates for  $H_s$  are higher for the 50-year extreme values in winter over a small area of the central GSL. Overall, the locations of projected increases and decreases in return values estimated by GEV are consistent with the GPD results; the variable amplitudes of projected return values estimated by GEV are similar with those estimated by the GPD. Therefore, the return values of extremes in  $H_s$  estimated by GPD are credible. Thus, the increases in return values of extremes in  $H_s$  in GSL, shown in Figs. 10 and 11, are cause for concern in terms of social-economic activities, like the maintenance of coastal and nearshore infrastructure and related issues.

## 7. Discussion and conclusions

We have investigated the wave climate, including the extreme waves, over the Gulf of St. Lawrence by using CRCM simulations to provide relatively high resolution winds to drive a modern operational wave model WAVEWATCHIII™, denoted WW3. By comparing WW3

results with the IOWAGA wave hindcast, we first show that the constructed wave climate for the present period can capture the spatial patterns of mean  $H_s$ , mean 10% highest and the maximum  $H_s$  well, in both summer and winter. Moreover, we show that CRCM can reproduce the track density of extratropical cyclones well in the North Atlantic in these two seasons; moreover, the sea ice concentrations over the GSL driven by NEMO are simulated well, in winter (Long et al., 2015). This provides confidence in model projections of both wave climate changes over the GSL and possible impacts of climate change on the waves under a warmer climate scenario.

Under the SRES A1B scenario from IPCC (2007), the WW3 simulations driven by winds from CRCM outputs suggest that projected changes in wave climate have seasonal differences. In summer, the mean  $H_s$ , mean 10% highest  $H_s$ , and the maximum  $H_s$  are expected to decrease for nearly the entire GSL whereas the associated values for winter are projected to increase over almost the entire GSL. These seasonal variations with respect to climate change can be related to particular climate change characteristics, such as storms and sea ice properties in the GSL.

In summer, projected decreases in mean  $H_s$ , mean 10% highest  $H_s$  and the maximum  $H_s$  are linked to decreases in cyclone track density in

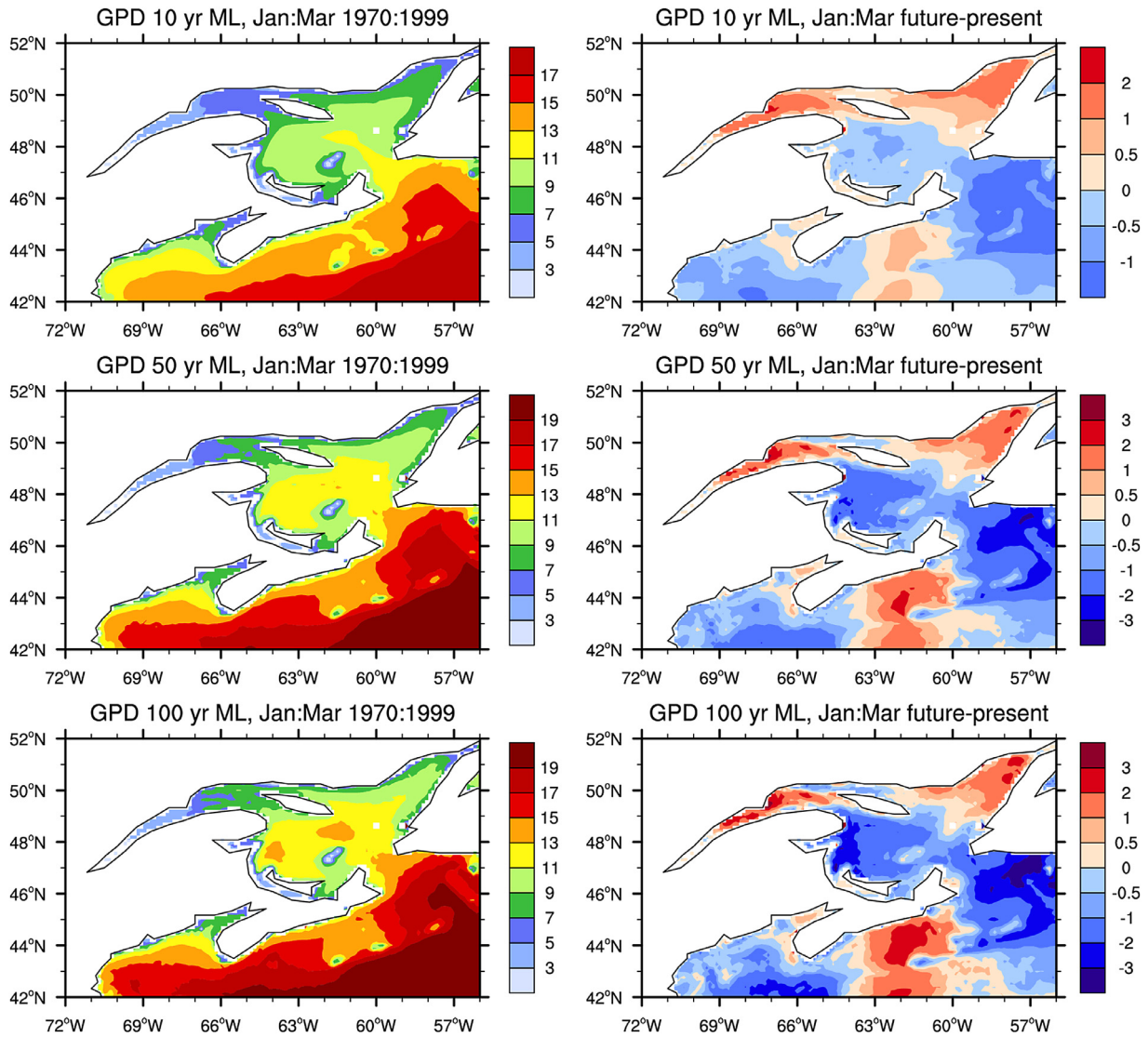


Fig. 11. As in Fig. 10, for the winter season.

the GSL. In winter, the effects of changes in the cyclone climate on wave climate in GSL in the future change scenario are expected to be small because the cyclone track density is projected to slightly decrease in the GSL. These effects are mitigated by competing climate factors, namely sea ice. The impacts of climate change causing reductions in ice are expected to be an important factor related to increases in the mean  $H_s$ , mean 10% highest and the maximum  $H_s$  values in the GSL in winter. Expected reductions in ice allow more open water for waves to be generated and to grow, whereas in former decades, the GSL was frozen in winter. Thus, changes in sea ice are consistent with increases in the wave climate.

In terms of the extreme wave analysis for the GSL, we show that the GPD distribution provides a better fit for the extreme  $H_s$  values than the GEV distribution, in both summer and winter. Comparing a statistical analysis based on different thresholds (95% and 97% percentile) and three methods (MPS, ML and PWM) for parameter estimation, the 95% percentile threshold and the ML method in GPD are treated as the best choice to fit the distribution of extreme  $H_s$  values and to estimate the return values. The spatial patterns of estimated 10-, 50- and 100-year extreme values for  $H_s$  are similar to each other, respectively, and are characterized by the gradient decreases from the offshore open ocean waters to the coastal areas.

In summer, the return values for  $H_s$  over the western coastal area of

the GSL are around 0–6 m for the 10-year return value for  $H_s$  and around 0–7 for the 50- and 100-year extreme values. Return values for the northern GSL area are higher than those for the western coastal area, with values between 5–7 m. In the central GSL, the largest values are relatively high, estimated as 9 m, 10 m and 11 m for return values in  $H_s$ . Under the A1B scenario, results obtained from WW3 simulations of waves suggest that the return values of  $H_s$  will decrease over the eastern part of GSL and increase over small areas of the St. Lawrence Estuary, Jacques Cartier Strait and southwestern part of GSL. The projected changes in the return values of extremes in  $H_s$  in these areas are consistent with the associated changes in the maximum  $H_s$  values over most of the GSL, although covering a relatively larger area for the increases in return values of  $H_s$ .

In winter, the return values over the St. Lawrence Estuary and southwestern portion of the GSL are around 0–5 m and over the northern GSL, around 5–9 m. In the central GSL, for 10-, 50- and 100-year extreme values in  $H_s$ , the largest values are up to 11 m, 11 m and 13 m, respectively. In the future climate scenario, the projected increases in return values are mostly concentrated in the St. Lawrence Estuary, the northern part, and the southwestern GSL, which is consistent with changes in the maximum  $H_s$  in these regions.

In this paper, a qualitative analysis using a single model simulation is performed to estimate possible future climate change. The results are

qualitative in that they are similar to what would be obtained using a larger ensemble of simulations. However, within a large ensemble of simulations, uncertainty varies from one member of the ensemble to another, and thus the entire ensemble needs to be calculated in order to accurately estimate the uncertainty for a particular given member of the ensemble. Presently, for any given IPCC climate change scenario, many climate projection studies are based on multi-model ensembles. A discussion of the application and development of multi-model ensembles for studies of climate change and the variance of results across different members of the ensemble may be found in IPCC (2007, 2013) and references therein. On average, the dominant source of uncertainty in the simulated climate response at middle and high latitudes is internal atmospheric variability, which is estimated to account for at least half of the inter-model spread in projected climate trends (Deser et al., 2012). In the Gulf of St. Lawrence, the uncertainties are generally larger for surface wind speeds than for surface air temperatures (SAT). For example, the variance of SAT changes is about 0.2 °C, which is about 10% of the SAT increase. However, the variance for projected changes in surface wind speed is about 0.2 m/s, which has the same magnitude as the projected changes, suggesting significant uncertainty in the projected changes in the surface wind speeds (Perrie et al., 2015). The uncertainties associated with the inter-model spread in the projections of the possible future wave height climate will need to be addressed in future studies.

## Acknowledgments

We thank the Panel on Energy Research and Development (PERD), the Aquatic Climate Change Adaptations Service Program (ACCASP), the Marine Environmental Observation Prediction and Response Network (MEOPAR), and the Northeast Regional Association of Coastal Ocean Observing Systems (NERACOOS) for supporting this work.

## References

- Ardhuin, F., Rogers, E., Babanin, AV., Filipot, JF., Magne, R., Roland, A., van der Westhuysen, A., Queffelec, P., Lefevre, JM., Aouf, L., Collard, F., 2010. Semiempirical dissipation source functions for ocean waves. Part I: definition, calibration, and validation. *J. Phys. Oceanogr.* 40, 1917–1941. <http://dx.doi.org/10.1175/2010JP04324.1>.
- Bengtsson, L., Hodges, KI., Roeckner, E., 2006. Storm tracks and climate change. *J. Clim.* 19, 3518–3543. <http://dx.doi.org/10.1175/JCLI3815.1>.
- Bouillon, S., Morales Maqueda, MA., Legat, V., Fichefet, T., 2009. An elastic-viscous-plastic sea ice model formulated on Arakawa B and C grids. *Ocean Model.* 27, 174–184. <https://doi.org/10.1016/j.ocemod.2009.01.004>.
- Brickman, D., Drozdowski, A., 2012. Development and Validation of a Regional Shelf Model for Maritime Canada Based on the NEMO-OPA Circulation Model. Canadian Technical Report of Hydrography and Ocean Sciences. 278 Published by Fisheries and Oceans Canada. vii–57 pp. Retrieved from <http://www.dfo-mpo.gc.ca/Library/347377.pdf>.
- Caries, S., Sterl, A., 2005. 100-year return value estimates for ocean wind speed and significant wave height from the ERA-40 data. *J. Clim.* 18, 1032–1048. <http://dx.doi.org/10.1175/JCLI3312.1>.
- Caya, D., Biner, S., 2004. Internal variability of RCM simulations over an annual cycle. *Clim. Dyn.* 22, 33–46. <https://doi.org/10.1007/s00382-003-0360-2>.
- Caya, D., Laprise, R., 1999. A semi-implicit semi-Lagrangian regional climate model: the Canadian RCM. *Mon. Weather Rev.* 127, 341–362. [http://dx.doi.org/10.1175/1520-0493\(1999\)127<0341:ASISLR>2.0.CO;2](http://dx.doi.org/10.1175/1520-0493(1999)127<0341:ASISLR>2.0.CO;2).
- Coles, S., 2001. *An Introduction to Statistical Modeling of Extreme Values*. Springer, London, pp. 208.
- Dee, DP., Uppala, SM., Simmons, AJ., Berrisford, P., Poli, P., Kobayashi, S., Andrae, U., Balmaseda, MA., Balsamo, G., Bauer, P., Bechtold, P., Beljaars, ACM., van de Berg, L., Bidlot, J., Bormann, N., Delsol, C., Dragani, R., Fuentes, M., Geer, AJ., Haimberger, L., Healy, SB., Hersbach, H., Hólm, EV., Isaksen, I., Kållberg, P., Köhler, M., Matricardi, M., McNally, AP., Monge-Sanz, BM., Morcrette, J.-J., Park, B.-K., Peubey, C., de Rosnay, P., Tavolato, C., Thépaut, J.-N., Vitart, F., 2011. The ERA-interim reanalysis: configuration and performance of the data assimilation system. *Q. J. R. Meteorol. Soc.* 137, 553–597. <https://doi.org/10.1002/qj.828>.
- Deser, C., Phillips, A., Bourdette, V., Teng, H., 2012. Uncertainty in climate change projections: the role of internal variability. *Climate Dynamics* 38. <https://doi.org/10.1007/s00382-010-0977-x>.
- Fichefet, T., Morales Maqueda, MA., 1997. Sensitivity of a global sea ice model to the treatment of ice thermodynamics and dynamics. *J. Geophys. Res.* 102 (12), 609–612. <https://doi.org/10.1029/97JC00480>.
- Fischer-Bruns, I., von Storch, H., González-Rouco, JF., Zorita, E., 2005. Modelling the variability of midlatitude storm activity on decadal to century time scales. *Clim. Dyn.* 25, 461–476. <https://doi.org/10.1007/s00382-005-0036-1>.
- Gal-Chen, T., Somerville, R., 1975. On the use of a coordinate transformation for the solution of the Navier–Stokes equations. *J. Comput. Phys.* 17, 209–228. [http://dx.doi.org/10.1016/0021-9991\(75\)90037-6](http://dx.doi.org/10.1016/0021-9991(75)90037-6).
- Gallagher, S., Gleeson, E., Tiron, R., McGrath, R., Dias, F., 2016. Twenty-first century wave climate projections for Ireland and surface winds in the North Atlantic Ocean. *Adv. Sci. Res.* 13, 75–80. <https://doi.org/10.5194/asr-13-75-2016>.
- Goda, Y., 2010. *Random sea and design of maritime structures*. 2nd ed. *Advanced Series on Ocean Engineering*. World Scientific, Singapore.
- Grabemann, I., Weisse, R., 2008. Climate change impact on extreme wave conditions in the North Sea: an ensemble study. *Ocean Dyn.* 58, 199–212. <https://doi.org/10.1007/s10236-008-0141-x>.
- Guo, L., Perrie, W., Long, Z., Toulany, B., Sheng, J., 2015. The impacts of climate change on the autumn North Atlantic wave climate. *Atmos.-Ocean* 53, 491–509. <https://doi.org/10.1080/07055900.2015.1103697>.
- Guo, L., Sheng, J., 2015. Statistical estimation of extreme ocean waves over the eastern Canadian shelf from 30-year numerical wave simulation. *Ocean Dyn.* 65, 1489–1507. <https://doi.org/10.1007/s10236-015-0878-y>.
- IPCC (Intergovernmental Panel on Climate Change), 2007. Summary for policymakers. In: *Climate Change 2007: The Physical Science Basis*. Contribution of Working Group I to the Fourth Assessment Report of the Intergovernmental Panel on Climate Change (pp. 1–18). Solomon S., Qin D., Manning M., Chen Z., Marquis M., Averyt K., Tignor M., Miller H.L. (eds.). Cambridge University Press, Cambridge, United Kingdom and New York, NY, USA.
- IPCC, 2013. *Climate Change 2013: The Physical Science Basis*. Contribution of Working Group I to the Fifth Assessment Report of the Intergovernmental Panel on Climate Change. Stocker TF, Qin D, Plattner GK, Tignor M, Allen SK, Boschung J, Nauels A, Xia Y, Bex V, Midgley PM (eds.). Cambridge University Press, Cambridge, United Kingdom and New York, NY, USA, 1535 pp. doi:10.1017/CBO9781107415324.
- Jung, T., Gulev, SK., Rudeva, I., Soloviev, V., 2006. Sensitivity of extratropical cyclone characteristics to horizontal resolution in the ECMWF model. *Q. J. R. Meteorol. Soc.* 132, 1839–1857. <https://doi.org/10.1256/qj.05.212>.
- Kharif, C., Giovanangeli, J.-P., Touboul, J., Grare, L., Pelinovsky, E., 2008. Influence of wind on extreme wave events: experimental and numerical approaches. *J. Fluid Mech.* 594, 209–247. <https://doi.org/10.1017/S0022212007009019>.
- Knippertz, P., Ulbrich, U., Speth, P., 2000. Changing cyclones and surface wind speeds over the North Atlantic and Europe in a transient GHG experiment. *Clim. Res.* 15, 109–122. <https://doi.org/10.3354/cr015109>.
- Laprise, R., Caya, D., Frigon, A., Paquin, D., 2003. Current and perturbed climate as simulated by the second-generation Canadian Regional Climate Model (CRCM-II) over northwestern North America. *Clim. Dyn.* 21, 405–421. <https://doi.org/10.1007/s00382-003-0342-4>.
- Liu, Q., Babanin, A., Fan, Y., Zieger, S., Guan, C., Moon I.-I., 2017. Numerical simulations of ocean surface waves under hurricane conditions: assessment of existing model performance. *Ocean Model.* 118, 73–93.
- Long, Z., Perrie, W., Chassé, J., Brickman, D., Guo, L., Drozdowski, A., Hu, H., 2015. Impacts of climate change in the Gulf of St. Lawrence. *Atmos.-Ocean* 54, 337–351. <https://doi.org/10.1080/07055900.2015.1029869>.
- Lorenz, DJ., DeWeaver, ET., 2007. Tropopause height and zonal wind response to global warming in the IPCC scenario integrations. *J. Geophys. Res.* 112, D10119. <https://doi.org/10.1029/2006JD008087>.
- Madeç, G., Delecluse, P., Imbard, M., Lévy, C., 1998. OPA 8.1 ocean general circulation model reference manual, No. 11. Note Du Pôle de Modélisation. Institut Pierre-Simon Laplace (IPSL), France.
- McInnes, KL., Erwin, TA., Bathols, JM., 2011. Global Climate Model projected changes in 10m wind speed and direction due to anthropogenic climate change. *Atmos. Sci. Lett.* 12, 325–333. <https://doi.org/10.1002/asl.341>.
- Menéndez, M., Méndez, FJ., Izaguirre, C., Luceño, A., Losada, IJ., 2009. The influence of seasonality on estimating return values of significant wave height. *Coast. Eng.* 56, 211–219. <http://dx.doi.org/10.1016/j.coastaleng.2008.07.004>.
- Murray, RJ., Simmonds, I., 1991a. A numerical scheme for tracking cyclone centres from digital data. Part I: development and operation of the scheme. *Aust. Meteor. Mag.* 39, 155–166. <http://stormtrack.ouranos.ca/Ref/Murray.pdf>.
- Murray, RJ., Simmonds, I., 1991b. A numerical scheme for tracking cyclone centres from digital data. Part II: application to January and July general circulation model simulations. *Aust. Meteor. Mag.* 39, 167–180.
- Nakićenović, N., Alcamo, J., Davis, G., de Vries, B., Fenhann, J., Gaffin, S., Gregory, K., Gruebler, A., Jung, TY., Kram, T., Lebre La Rovere, E., Michaelis, L., Mori, S., Morita, T., Pepper, W., Pitcher, H., Price, L., Riahi, K., Roehrl, A., Rogner, H.-H., Sankovski, A., Schlesinger, M., Shukla, P., Smith, S., Swart, R., Van Rooijen, S., Victor, N., Dadi, Z., 2000. *Special Report on Emissions Scenarios: A Special Report of Working Group III of the Intergovernmental Panel on Climate Change*. Cambridge University Press, Cambridge, UK.
- Neu, U., Akperov, MG., Bellenbaum, N., Benestad, R., Blender, R., Caballero, R., Coccozza, A., Dacre, HF., Feng, Y., Fraedrich, K., Gieger, J., Gulev, S., Hanley, J., Hewson, T., Inatsu, M., Keay, K., Kew, SF., Kindem, I., Leckebusch, GC., Liberato, M., Lionello, P., Mokhov II., Pinto, JG., Raible, CC., Reale, M., Rudeva, I., Schuster, M., Simmonds, I., Sinclair, M., Sprenger, M., Tilinina, ND., Trigo, IF., Ulbrich, S., Ulbrich, U., Wang, XL., Wernli, H., 2013. IMILAST: a community effort to intercompare extratropical cyclone detection and tracking algorithms. *Bull. Am. Meteorol. Soc.* 94, 529–547. <http://dx.doi.org/10.1175/BAMS-D-11-00154.1>.
- Peng, G., Meier, WN., Scott, DJ., Savoie, MH., 2013. A long-term and reproducible passive microwave sea ice concentration data record for climate studies and monitoring. *Earth Syst. Sci. Data* 5, 311–318. <https://doi.org/10.5194/essd-5-311-2013>.
- Perrie, W., Long, Z., Chassé, J., Blokhina, M., Guo, L., Hu, H., 2015. Projected changes in surface air temperature and surface wind in the Gulf of St. Lawrence. *Atmos.-Ocean*,



- 53 (5), 571–581. <https://doi.org/10.1080/07055900.2015.1086295>.
- Raible, CC, Della-Marta, PM, Schwierz, C, Wernli, H, Blender, R, 2008. Northern Hemisphere extratropical cyclones: a comparison of detection and tracking methods and different reanalyses. *Mon. Weather Rev.* 136, 880–897. <http://dx.doi.org/10.1175/2007MWR2143.1>.
- Raschle, N, Ardhuin, F, 2013. A global wave parameter database for geophysical applications. Part 2: model validation with improved source term parameterization. *Ocean Model.* 70, 174–188. <http://dx.doi.org/10.1016/j.ocemod.2012.12.001>.
- Riette S, Caya D. 2002. Sensitivity of short simulations to the various parameters in the new CRCM spectral nudging. *Res. Act. Atmos. Ocean. Model.*, H. Ritchie (Ed.), WMO/TD – No. 1105, Report No. 32: pp. 7.39–7.40.
- Ruest, B, Neumeier, U, Dumont, D, Bismuth, E, Senneville, S, Caveen, J, 2016. Recent wave climate and expected future changes in the seasonally ice-infested waters of the Gulf of St. Lawrence, Canada. *Clim. Dyn.* 46 (1–2), 449–466. <https://doi.org/10.1007/s00382-015-2592-3>.
- Ruest, B, Neumeier, U, Dumont, D, Lambert, A, 2013. Wave climate evaluation in the Gulf of St. Lawrence with a parametric wave model. *Coast. Dyn.* 1363–1374. [http://www.coastaldynamics2013.fr/pdf\\_files/132\\_Ruest\\_Benoit.pdf](http://www.coastaldynamics2013.fr/pdf_files/132_Ruest_Benoit.pdf).
- Shen, H, Perrie, W, Hu, Y, He, Y, 2018. Remote sensing of waves propagating in the marginal ice zone by SAR. *J. Geophys. Res.* <https://doi.org/10.1002/2017JC013148>. First published: 27 December 2017.
- Simmonds, I, Murray, RJ, 1999. Southern extratropical cyclone behavior in ECMWF analyses during the FROST special observing periods. *Weather Forecast.* 14, 878–891. [http://dx.doi.org/10.1175/1520-0434\(1999\)014<0878:SECBIE>2.0.CO;2](http://dx.doi.org/10.1175/1520-0434(1999)014<0878:SECBIE>2.0.CO;2).
- Strachan, J, Vidale, PL, Hodges, K, Roberts, M, Demory, M-E, 2013. Investigating global tropical cyclone activity with a hierarchy of AGCMs: the role of model resolution. *J. Clim.* 26, 133–152. <http://dx.doi.org/10.1175/JCLI-D-12-00012.1>.
- Swail, VR, Cardone, VJ, Ferguson, M, Gummer, DJ, Harris, EL, Orelup, EA, Cox, AT, 2006. The MSC50 wind and wave reanalysis. In: *Proceedings of the 9th International Workshop on Wave Hindcasting and Forecasting*. Victoria, BC, Canada.
- Tanguay, M, Robert, A, Laprise, R, 1990. A semi-implicit semi-Lagrangian fully compressible regional forecast model. *Mon. Weather Rev.* 118, 1970–1980. [http://dx.doi.org/10.1175/1520-0493\(1990\)118<1970:ASISLF>2.0.CO;2](http://dx.doi.org/10.1175/1520-0493(1990)118<1970:ASISLF>2.0.CO;2).
- Teena, NV, Kumar, VS, Sudheesh, K, Sajeev, R, 2012. Statistical analysis on extreme wave height. *Nat. Hazards* 64, 223–236. <https://doi.org/10.1007/s11069-012-0229-y>.
- Thomson, J, Fan, Y, Stammerjohn, S, Stopa, J, Rogers, WE, Girard-Ardhuin, F, Ardhuin, F, Shen, H, Perrie, W, Shen, H, Ackley, S, Babanin, A, Liu, Q, Guest, P, Maksym, T, Wadhams, P, Fairall, C, Persson, O, Doble, M, Graber, H, Lund, B, Squire, V, Gemmrich, J, Lehner, S, Holt, B, Meylan, M, Brozena, J, Bidlot, J-R, 2016. Emerging trends in the sea state of the Beaufort and Chukchi seas. *Ocean Model.* 105, 1–12. <https://doi.org/10.1016/j.ocemod.2016.02.009>.
- Tolman, HL, 2003. Treatment of unresolved islands and ice in wind wave models. *Ocean Model.* 5, 219–231.
- Tolman HL. (2009). User Manual and System Documentation of WAVEWATCH III™ Version 3.14. Technical Note 276. Camp Springs, MD: NOAA, USA. [http://nopp.ncep.noaa.gov/mmab/papers/tm276/MMAB\\_276.pdf](http://nopp.ncep.noaa.gov/mmab/papers/tm276/MMAB_276.pdf).
- Tolman, HL, Balasubramanian, B, Burroughs, LD, Chalikov, DV, Chao, YY, Chen, HS, Gerald, VM, 2002. Development and implementation of wind-generated ocean surface wave models at NCEP. *Weather Forecast.* 17, 311–333. [http://dx.doi.org/10.1175/1520-0434\(2002\)017<0311:DAIOWG>2.0.CO;2](http://dx.doi.org/10.1175/1520-0434(2002)017<0311:DAIOWG>2.0.CO;2).
- Wang, XL, Feng, Y, Swail, VR, 2012. North Atlantic wave height trends as reconstructed from the 20th century reanalysis. *Geophys. Res. Lett.* 39, L18705. <https://doi.org/10.1029/2012GL053381>.
- Wang, XL, Swail, VR, 2006. Climate change signal and uncertainty in projections of ocean wave heights. *Clim. Dyn.* 26, 109–126. <https://doi.org/10.1007/s00382-005-0080-x>.
- Wolf, J, Woolf, DK, 2006. Waves and climate change in the north-east Atlantic. *Geophys. Res. Lett.* 33, L06604. <https://doi.org/10.1029/2005GL025113>.
- Yin, JH, 2005. A consistent poleward shift of the storm tracks in simulations of 21st century climate. *Geophys. Res. Lett.* 32, L18701. <https://doi.org/10.1029/2005GL023684>.